Cryo-SEM Reveals Native Architecture and Matrix Complexity in *P. aeruginosa* Biofilms

Osondu-Chuka Goodness O.[1], Schandl Stephan[2], Guruprakash Subbiahdoss[1], Aleksandr Ovsianikov[2], Olivier Guillaume[2] and Reimhult Erik[1]

[1]Institute of Colloid and Biointerface Science, BOKU University, Muthgasse 11, Vienna 1190, Austria. [2] Institute of Materials Science and Technology, Technische Universität Wien, Vienna, Austria.

Abstract

Pseudomonas aeruginosa biofilms pose a critical challenge in clinical settings due to their high resistance to antibiotics and immune clearance, primarily attributed to the protective extracellular matrix (ECM). Accurate visualization of biofilm structure in its native state is crucial for understanding its resilience and guiding the development of targeted therapeutics. We used three different sample preparation methods - critical-point drying (CPD), air-drying (AD), and high-pressure cryogenic freezing for the sample preparation of native biofilms grown on solid substrates and microcolonies grown within alginate matrices. Our goal was to compare their morphologies and spatial organizations using SEM and cryogenic SEM (cryo-SEM). Cryo-SEM revealed *Pseudomonas* biofilms as highly hydrated, organized structures, preserving delicate ECM features and cellular morphology. The ECM and cell distributions were severely distorted in CPD and air-dried samples due to dehydration. Notably, cryo-SEM revealed that mucoid *P. aeruginosa* grown for 4 days is spatially separated and short-range ordered in the extensive ECM with nearest-neighbor distances averaging 1.26 µm, while PAO1 showed a broader distribution in nearest-neighbor distances with an average of 1.64 µm, both challenging the view of biofilms as closely packed cell aggregates. Furthermore, distinct differences in cryo-SEM-visualized ECM structure were observed between PAO1 and mucoid strains. The latter formed a voluminous, filamentous matrix rich in aligned fibrillar ultrastructures, which likely derive from protein ECM components. In contrast, PAO1 displayed denser biofilms with mesh-like ECMs and higher cell densities. The cell densities of both biofilms were observed to be lowest close to the substrate. While PAO1 displays a monotonic increase in cell density from the substrate to the biofilm surface, mucoid biofilms displayed a stratified pattern, with significantly higher densities at the surface and mid-depth than near the substrate. Our findings establish cryo-SEM as a superior method for high-fidelity imaging of biofilms, offering new insights into the structural organization of cells and ECM in *P. aeruginosa* biofilms.

1.0 Introduction

Pseudomonas aeruginosa (PA) is a highly adaptable, opportunistic pathogen known for its ability to form robust biofilms, which contribute to persistent infections and antibiotic resistance.[1–3] Central to this resilience is the biofilm's extracellular matrix (ECM), a complex network of polysaccharides (alginate, Pel, and Psl), proteins, and extracellular DNA (eDNA) that acts as a robust protective barrier, enabling bacteria to withstand high antibiotic concentrations.[4,5] Alginate, in particular, is a hallmark of mucoid clinical isolates, often found in cystic fibrosis (CF) lungs, where it enhances biofilm resilience.[4,6–8] This resilience is primarily attributed to its ability to provide structural stability and act as a physical barrier against both antibiotics and host immune defenses.[4,6,8] Overproduction of alginate leads to biofilms that are notably persistent and difficult to eradicate in clinical settings, making it a critical target for research.[6,7] Understanding the structural complexity of these biofilms is therefore essential for developing effective therapeutic strategies, as biofilm formation by PA plays a central role in chronic infections, such as those associated with CF, burn wounds, and indwelling medical devices.[4,9]

In addition to studying clinical biofilms or biofilms grown *in vitro*, various *in vitro* models have been developed using alginate hydrogels to encapsulate bacteria.[10,11] These bacteria-loaded alginate hydrogel models mimic key features of the mucoid biofilm phenotype observed in clinical settings, particularly in CF lungs.[10,12] These models can help dissecting the specific role of alginate in biofilm architecture and resilience, thus advancing our understanding of mucoid biofilms.

Electron microscopy has long been employed in biological research to visualize the ultrastructure of cells, bacteria, and tissues. Among its variants, scanning electron microscopy (SEM) has emerged as a valuable tool for visualizing PA biofilms, providing high-resolution images that reveal intricate surface morphology and spatial organization.[13–15] It has been particularly useful for examining biofilms formed on medical devices, where PA establishes resilient communities.[16,17] However, biofilm hydration and complex extracellular matrix composition, particularly with polysaccharide-rich regions,[18–20] pose a significant challenge in electron microscopy, where traditional methods require sample dehydration, leading to structural collapse and loss of integrity.[21–23] This results from the removal of water in the structure and from the changed energetics of structures favored by hydration and ionic interactions, which are no longer in equilibrium when the water is removed. Membranes and polysaccharides suffer from significant reorganization, shrinkage, and collapse when water is removed, distorting their native architecture and functional properties.[19,24,25] Specialized sample preparation and imaging techniques are therefore necessary to visualize the native architecture of biofilms without introducing structural artifacts.[14,19,26] Additionally, standard

SEM techniques are limited to imaging the surface of biofilms, which restricts our ability to understand the organization within the biofilm, as it may differ significantly from the surface structure and cell distribution. A reasonable assumption is that biofilms change their composition as they grow, thereby altering their structure with distance from the substrate on which they are growing.[27,28] Techniques that expose the organization within the biofilm to compare it to the structure in the presumably faster-growing top part are therefore essential in understanding the biofilm architecture.

Several preparation techniques have been developed to address the challenge of imaging hydrated biological structures.[18,19,22] Controlled drying by the critical-point drying (CPD) method has been widely used to preserve cellular morphology; however, it introduces artifacts in highly hydrated structures, such as biofilms.[29,30] Fixation, commonly used to stabilize biological samples for electron microscopy, presents another limitation. While chemical fixatives, such as aldehydes and osmium tetroxide, cross-link cellular components, they do not preserve the organization of polysaccharides and other sugar-rich structures.[23,31] The dehydration steps required for fixation-based protocols further disrupt biofilm organization and shrink structures, making capturing the biofilm ultrastructure dubious. [23,29,30]

Cryo-scanning electron microscopy (cryo-SEM) offers a promising solution for preserving biofilm structures in their near-native state.[21,22] Rapid freezing of samples within milliseconds prevents ice crystal formation. Cryo-SEM preserves hydration by maintaining samples in a frozen, vitrified state, enabling high-resolution imaging of biofilms with minimal structural distortion.[19,32] This approach minimizes artifacts and provides a more accurate representation of biofilm morphology, capturing delicate extracellular polymeric substances (EPS) and cellular arrangements that are often lost with traditional preparation methods.[19,21,33] High-pressure freezing (HPF) applies mechanical pressure during freezing to reduce ice crystal growth, enabling deeper penetration of the freezing process in thick biofilm samples.[34–36] After cryo-freezing, the sample can be split open by various methods to expose a surface on or within the biofilm. [22,37,38] Nevertheless, the resulting split surface lacks contrast for imaging the ultrastructure, although large structures such as membranes and fibers are exposed. Improved contrast is achieved by depositing a thin carbon-metal film, usually at an angle, which also stabilizes the interface for imaging. In an additional step before the carbon-metal film deposition, freeze-etching, which involves the controlled sublimation of a small amount of surface ice before imaging, can be used to further enhance contrast and reveal structural details that are otherwise obscured by frozen water layers.[22,39,40] These cryo-methods, when combined with SEM, enable researchers to explore biofilm architectures in their hydrated state at unequaled resolution, potentially offering novel and critical insights.

The aim of our work was to leverage cryo-SEM to image and analyze PA biofilms in their native state, minimizing preparation-induced artifacts and comparing the outcomes with those obtained using traditional preparation methods. By revealing the native structural organization of cells and ECM, we seek to provide missing structural information beyond genetic and biochemical information that could prove instrumental to, e.g., establishing the causes of biofilm tolerance to antibiotics and developing more effective anti-biofilm strategies.

2 Results and Discussion

2.1 Cryo-SEM Preserves Alginate Biofilm Model and Mucoid Biofilm Structures in Contrast to Dehydration Methods

SEM is a vacuum imaging technique, and structural observations of naturally hydrated systems can vary depending on sample preparation methods, which is highly relevant to the use of SEM in biofilm research. Alginate hydrogels have been proposed as models for antibiotic testing on mucoid PA biofilms.[9,41,42] Such alginate gels displayed notable differences in SEM depending on the sample preparation method: air-dried (AD), critical-point dried (CPD), or HPF-cryo-prepared. In the AD and CPD samples (**Figure 1A and B**), the alginate hydrogels appeared spongy and compact, with wrinkled morphology. The pore sizes generally ranged from ~0.1 – 0.35 µm (**Figure S1)**. Conversely, the cryo-prepared sample (**Figure 1**C) retained a markedly more hydrated and native-like appearance, maintaining a porous network (~0,3 µm – 0,55 µm) (**Figure S1**), which had significantly larger pores than both the AD and CPD prepared samples ($p \leq 0.05$). Similar results have been observed in the literature where alginate gels comprised irregular internal pore spaces that increased in size with decreasing alginate concentration.[43] The observed pore diameters ranged from 0.2 to 3.0 µm within a 0.3% (w/v) gel, and from 0.1 to 1.0 µm within a 0.6% (w/v) gel.[43] However, we cannot rule out that the observed pore size is already partly reflecting sublimation of water during the minimal etching performed to provide imaging contrast, as is likely given the orders of magnitude smaller pore sizes obtained from rheological testing and diffusion studies.[9,44]

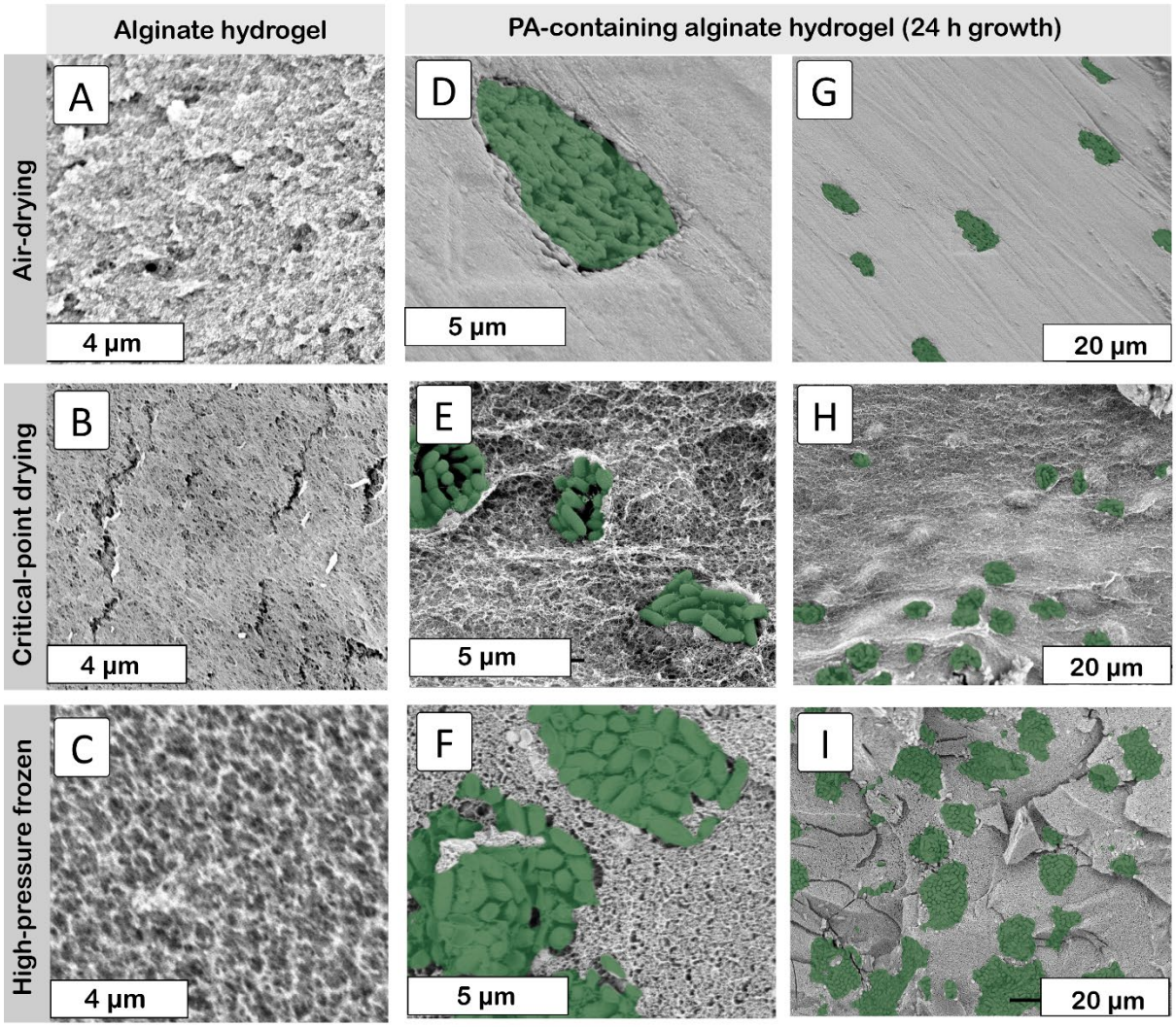

Figure 1: SEM micrographs depicting cross-sections of acetylated alginate hydrogels and biofilm models. Samples were prepared for imaging using air-drying (A, D, and G), critical-point drying (B, E, and H), and high-pressure freezing (etching time: 20 s – control alginate hydrogel, 40 s – PA-containing alginate hydrogel) (C, F, and I). A - C) acetylated alginate hydrogels, D - I) PAO1 encapsulated in acetylated alginate and grown overnight at 37 °C (biofilm models). The bacterial cells have been false-colored green for visibility.

In the next step, PA-containing alginate hydrogels (3D biofilm models) that closely mimic PA mucoid biofilms were studied after 24 h incubation at 37 °C.[41] As seen in **Figure 1 D and G**, biofilms from air-dried samples appeared collapsed and dense. Bacterial cells exhibited shrunken morphologies, and the alginate matrix lacked visible porosity, appearing as wrinkled sheaths. Samples prepared by CPD (**Figure 7E and H**) exhibited well-preserved cell morphologies and partly distorted matrices. While some shrinkage and compression were observed, the overall integrity of the alginate gel network and bacterial morphology was maintained compared to the air-

dried samples. In contrast, cryo-prepared samples (**Figure 7F and I**) revealed the high-resolution morphology of the alginate matrix and PA microcolonies, with cells embedded in a hydrated mesh-like alginate, as well as polymeric substances in the interstitial spaces between the cells. There is no obvious remodeling of the alginate matrix visible outside the microcolony.

Comparable insights on the growth and distribution of PA microcolonies in alginate hydrogel were obtained by Sønderholm et al., who studied PA aggregate formation within alginate bead models using confocal laser-scanning microscopy (CLSM).[42] However, the CLSM-based approach, while powerful for studying spatial organization and metabolic gradients in hydrated systems, lacks the ultrastructural resolution provided by cryo-SEM. In contrast, our imaging results reveal the fine details of bacterial morphology, the alginate hydrogel, and the matrix surrounding the bacteria, which are necessary to reveal differences in ultrastructure.

Figure 2 shows example SEM images of 4-day-old mucoid PA biofilms grown on type A gold carriers in Tryptic Soy Broth (TSB) and prepared for imaging with different methods: air-dried (AD), critical-point dried (CPD), and HPF-cryo-prepared. The characteristically rod-shaped PA have relatively intact shapes, without signs of collapse, indicating successful dehydration and preservation of cell structure from all preparation methods. However, in the AD samples (**Figure 2a**), the cells appear tightly packed with negligible visibility of the surrounding matrix. CPD-prepared samples (**Figure 2b**) suggest a dense and uneven spatial organization of PA cells in the biofilm.

In contrast, in cryo-prepared and cryo-SEM imaged samples **Figure 2c**), PA appear spatially organized as individual cells, embedded in a voluminous ECM, yet distinguishable, with some partially obscured by the ECM. The cryo-prepared biofilms retain a highly hydrated ECM structure, likely closely reflecting their native state, and with a morphology distinctly different from those observed in the cryo-prepared alginate model or observed with the other sample preparation techniques.

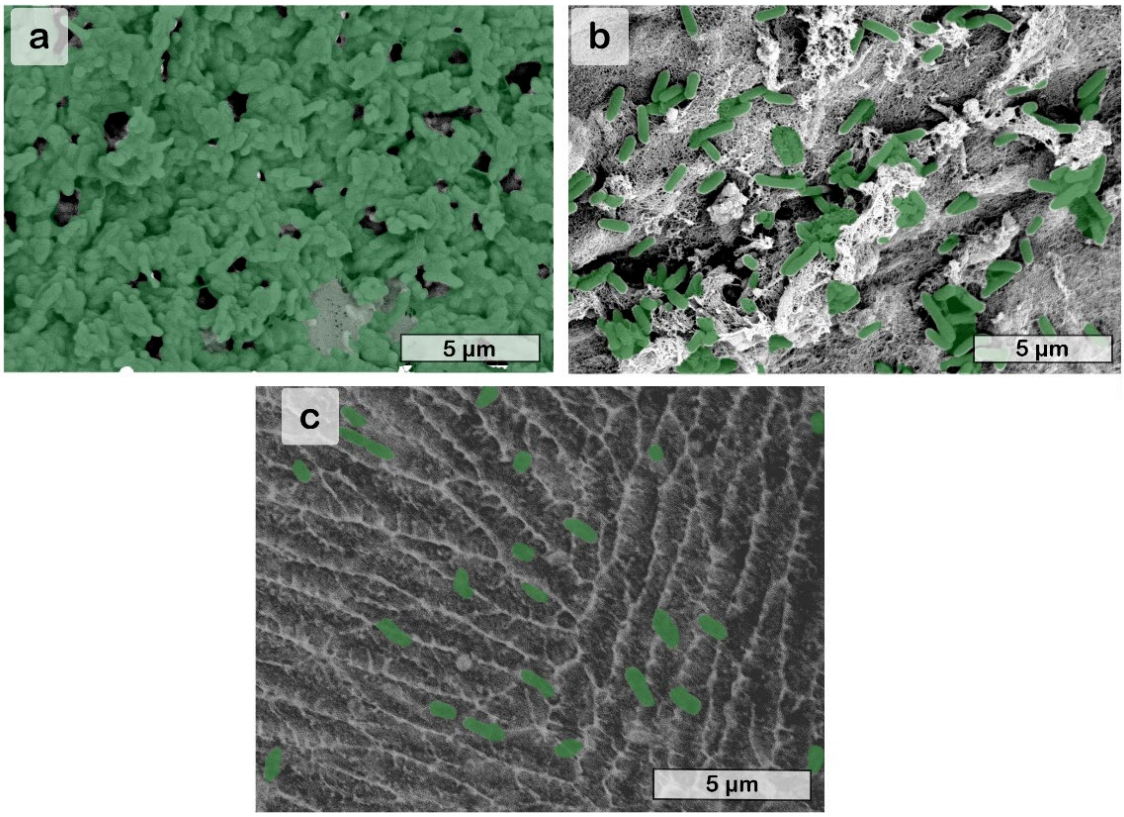

Figure 2: Scanning electron micrographs of the bulk region from 4-day-old mucoid PA biofilms grown in gold carriers. Samples were subsequently prepared for SEM by a) air drying, b) critical-point drying, and c) high-pressure cryo-freezing and subsequently fractured to reveal a plane within the bulk of the biofilms. The bacterial cells have been false-colored green for visibility.

The spatial organization differences observed between the different sample preparation methods applied to mucoid PA biofilms highlight important implications for interpreting biofilm organization and structure. As described in other studies,[45,46] AD and CPD methods can provide a clear visualization of bacterial cells, but these preparation methods misrepresent the actual structure of the native biofilm. The collapse and shrinkage observed in mucoid PA samples upon dehydration result in structural artifacts, such as cell clustering and loss of ECM ultrastructure. In contrast, HPF-prepared samples imaged by cryo-SEM conserve the organization. This finding is consistent with the work of Alhede *et al*., who compared cryo-methods with CPD, concluding that cryo-preparation of PAO1 biofilms preserves the matrix structure.[47] One striking novel observation from our study is the spatial organization and distribution of PA cells. As exemplified in **Figure 2**c, we find that mucoid PA biofilms consist of individual bacterial cells that are spatially separated but embedded within a continuous and protective ECM.

2.2 Cryo-SEM Enables Quantitative Determination of the Spatial Distribution of *P. aeruginosa* in Mucoid Biofilms

To quantify the distinct spatial organization observed in the cryo-prepared mucoid PA biofilms, we calculated the radial distribution function (RDF; g(r)) for the distribution of cells (**Figure 3**A). The variability between the images was low, as shown by the low standard error of the mean (SEM) in **Figure S2.** The RDF exhibits a striking short-range order, with a fitted Gaussian first-order peak at 1.26 µm and a full width at half maximum (FWHM) of 0.60 µm. There is a clear separation between the cells visible in the analyzed images, which in the RDF shows up as a gap size on the order of the cell dimension.

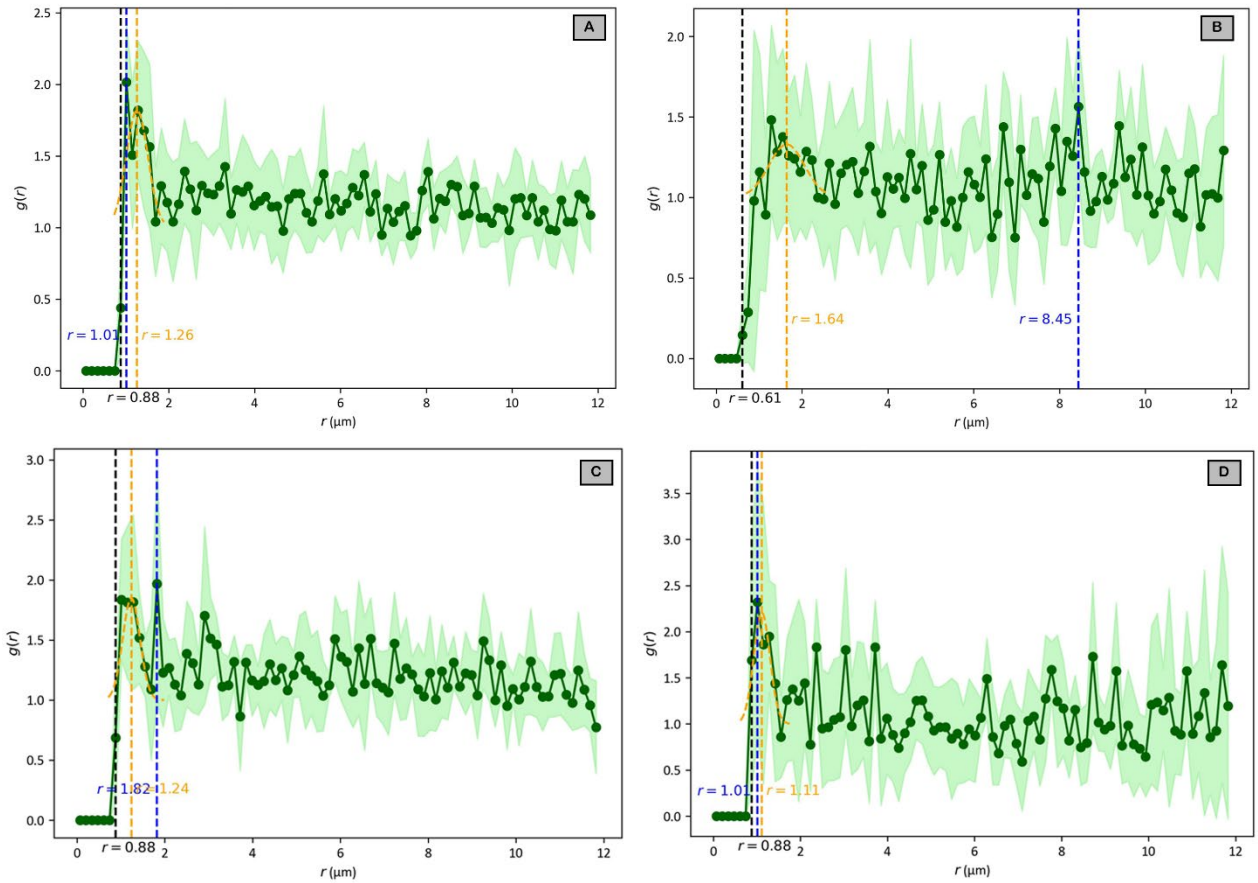

Figure 3: Averaged radial distribution function (RDF) analysis of PA biofilm spatial organization in cryo-SEM biofilm images, illustrating bacterial density as a function of radial distance from each cell center. A) bulk region of mucoid PA biofilm, B) bulk region of PAO1 biofilm. C) top region of mucoid PA biofilm, and D) bottom region of mucoid PA biofilm. 6 – 10 images per region were selected and used for the averaged RDF. The green line represents the mean RDF, while the shaded area indicates the 95% confidence interval (CI). The black, orange, and blue dashed lines mark the

minimum measured distance, the nearest-neighbor distance obtained by a Gaussian fit, and the most probable nearest-neighbor distance, respectively.

Having observed distinct cell–cell spacing in the bulk region of mucoid PA biofilms, we also examined the bulk region of PAO1 biofilms prepared under the same conditions as the mucoid PA biofilms. The PAO1 biofilms exhibited a more heterogeneous cell spacing in the bulk region. A Gaussian fit of the nearest neighbors gave a peak at 1.64 µm, indicating a slightly greater average nearest neighbor spacing than in the mucoid strain as well as a broader distribution (**Figure 3B**).

For the mucoid biofilm, we also analyzed the top and bottom regions separately (**Figure 3C and D**) to assess cell organization in these areas. The top region showed a local packing structure similar to that of the bulk, with a Gaussian fit peak at 1.24 µm. The bottom region, however, had slightly closer cell–cell spacing (Gaussian peak at 1.11 µm) and greater variability. The significance of this difference is uncertain but could be due to compression from overlying biomass, reflecting a higher early colonization density and growth, or changes in matrix density near the substrate.[48–50]

These observations challenge the conventional view of PA biofilms as tightly packed cell aggregates surrounded by ECM, which was mainly derived from the observation of collapsed biofilms.[51–54] An analogous finding of cell-cell spacing was reported by Kamila *et al.*, who described large distances between microbial cells in cryo-imaged *Staphylococcus epidermidis* and yeast biofilms but did not analyze it further.[22] A locally ordered, spaced, and homogeneous distribution of distant bacterial cells in biofilms has implications for our understanding of their communication, cooperation, and migration. In particular, it means that PA do not form microcolonies and that daughter cells are separated from their mother cells after cell division in these biofilms.

2.3 The Extracellular Matrix of Mucoid Biofilms Exhibits Aligned Fibrillar Structures in the Bulk and Mesh-Like Structures at the Surface

Cryo-SEM imaging of minimally freeze-etched mucoid PA biofilm samples revealed distinct structural variations between the top, bottom, and bulk regions of the biofilm (**Figure 4A – C and S4**). While the bulk region exhibited mostly locally aligned fibrils extending through the ECM (**Figure 4**C), the top and bottom parts of the biofilm displayed a markedly different ECM morphology. The top and bottom of the biofilm were characterized by a mesh-like appearance of the ECM (**Figure 4**A-B), although the bottom also prevalently displayed a fibrous but less aligned

structure (**Figure 4**B). This indicates a more fibrous, organized, and density-varied ultrastructure in the interior of mature biofilms than what is observed on their surface. We have not found such region-specific differences in ECM architecture between the upper, bulk, and bottom zones of mucoid PA biofilms reported in the literature, which can likely only be observed using HPF freeze-fracture cryo-SEM. Despite these differences in ECM ultrastructure, the spatial distribution of bacterial cells was homogeneous in all parts of the biofilms, showing no apparent clustering into microcolonies. The near equidistance of *P. aeruginosa* cells within all strata of the biofilms implies that the mechanism leading to their separation after division is either confined to the top layer of the biofilm and conserved as the biofilm expands or proceeds similarly throughout, where the latter would require active migration toward the biofilm surface if the cell density is equal throughout the biofilm.

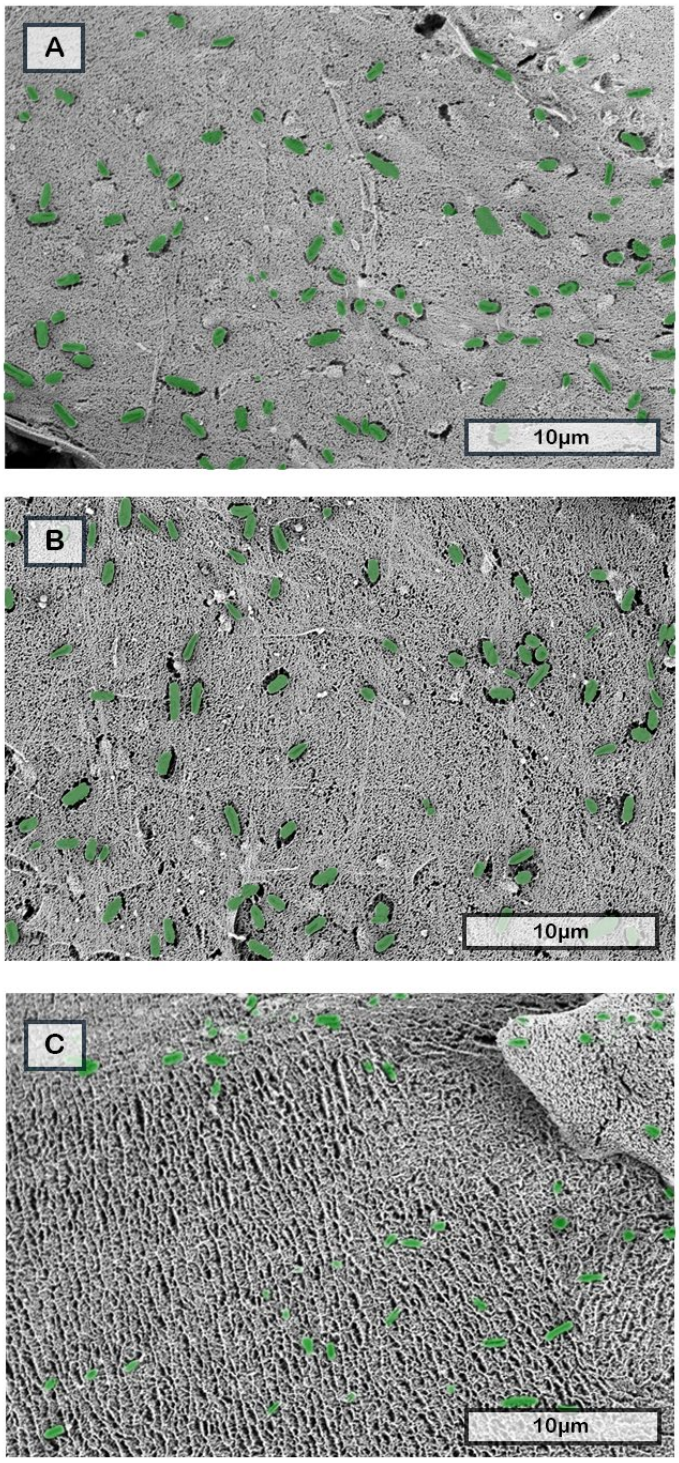

Figure 4: Cryo-SEM micrograph demonstrating variations in ECM architecture from different regions of a 4-day-old mucoid PA biofilm (~50 µm thick) grown on gold carriers. A) plane in the upper part of the biofilm (~1-5 µm from the biofilm surface), B) plane in the bottom part of the biofilm (~1-5 µm from the substrate), and C) plane in the bulk biofilm (~5 – 45 µm from the substrate).

2.4 Minimal Etching Preserves Mucoid Biofilm Ultrastructure, While Extended Etching Collapses It into a Mesh

Cryo-SEM imaging of PA mucoid biofilms (bulk region) subjected to varying etching times (0 s, 20 s, and 60 s) at –110 °C and ~5.6×10^{-7} mbar revealed progressive exposure of structural features (**Figure 5**). At 0 s etching, the biofilm surface appeared partially obscured by residual surface ice. Nonetheless, ECM contours and outlines of bacterial cells (yellow arrows) were discernible also where ice is visible (**Figure 5**A).

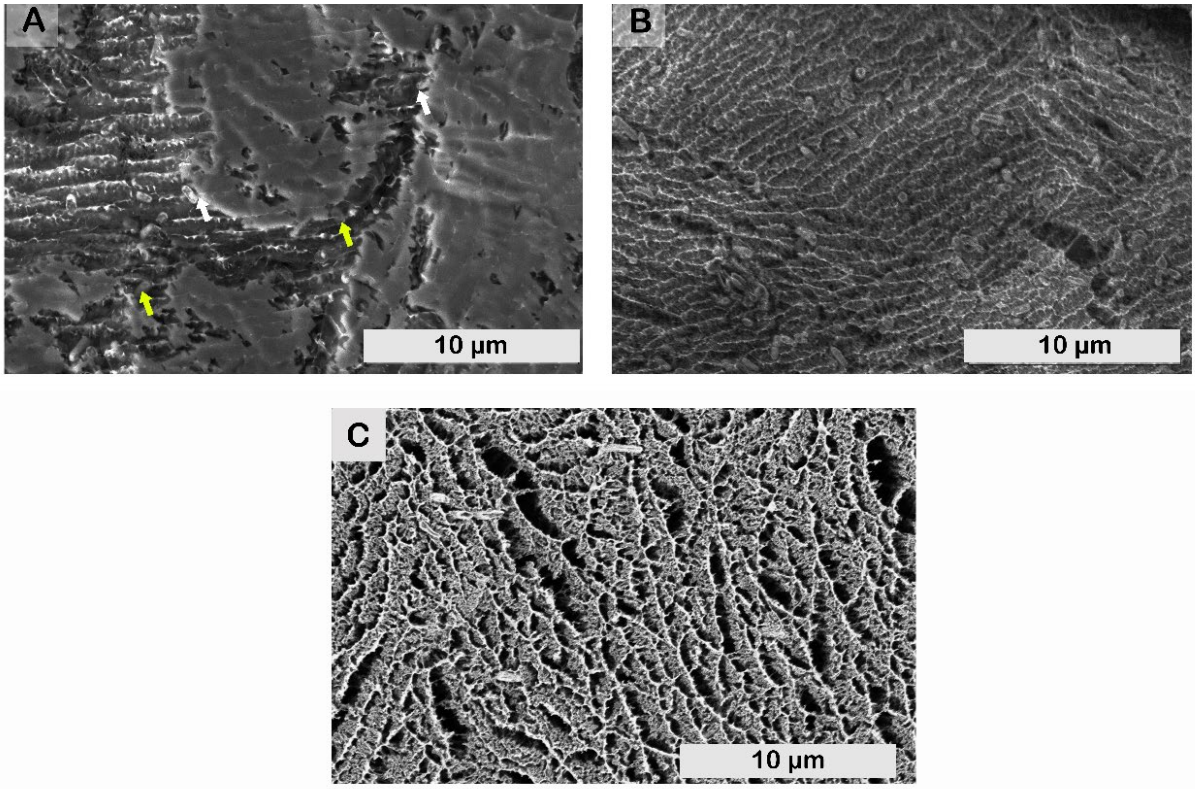

Figure 5: Cryo-SEM micrographs from the bulk region of 4-day-old mucoid PA biofilms. A) 0 s etching, B) 20 s etching, and C) deep etching (60 s). The yellow arrows indicate outlines of bacterial cells.

Etching for 20 s at -110 °C and ~5.6×10^{-7} mbar (**Figure 5B**) produced optimal surface contrast with well-preserved ultrastructure with good correspondence to the features imaged without etching. PA cells were visible and embedded in the ECM. The ECM in the bulk biofilm displayed aligned fibrillar features approximately 80 nm in width, with inter-fibrillar spacing ranging from 600 to 1000 nm. This etching duration appeared to achieve an effective balance between the removal of surface ice and the preservation of hydrated structural features of PA biofilms.

In contrast, extended etching for 60 s at -110°C and ~5.6×10^{-7} mbar (**Figure 5C**) led to sublimation of water to a greater depth, resulting in a more open and fibrous ECM morphology. Some pores appeared enlarged, reaching ~2 µm in diameter, and the ECM had increased fibrillar spacing in the range of 900 to 2000 nm, indicating the onset of matrix distortion and collapse. The fibrils were also less aligned and more mesh-like than after shorter etching times.

The observed effects of freeze-etching are consistent with studies by Wan *et al*., Dohnalkova *et al.*, and Garbarino *et al.*, which demonstrated that controlled etching could enhance the visualization of highly organized ultrastructural ECM and cellular features.[55–57] However, they also showed that extended etching times increased the risk of ECM ultrastructure alterations, which are particularly severe for strongly glycosylated (hydrated) ECMs,[56,57] such as what is found in mucoid PA biofilms.[58] Consistently in our study and theirs,[57] water removal *via* sublimation leads to a more mesh-like structure commonly associated with biofilm ECMs from a tentatively more organized and fibrous structure observed at near-full hydration.

2.5 Mucoid PA Biofilms Possess a Unique Ultrastructure with Aligned Fibrils

Different PA strains do not form the same types of biofilms.[59–61] Well-known examples include the dense biofilms formed on biomaterial surfaces where PA acts as an opportunistic pathogen and the mucoid biofilms formed by PA in cystic fibrosis patients.[53,62,63] Despite the differences in structure and the critical role of the ECM in shaping biofilm architecture and contributing to antimicrobial resistance, a notable gap remains in our understanding of the ultrastructural organization of different types of biofilms. Electron microscopy studies on PA have focused on bacterial cell morphology, surface attachment, or overall biofilm structure.[25,64,65] Differences in internal structure between biofilms, e.g., PAO1 *vs*. mucoid PA, have not been imaged and compared in detail.

After observing the fibrillar organization in mucoid PA biofilms, we compared these biofilms with PAO1 biofilms. Structural differences between these two strains were revealed, as seen in **Figure 6**. The ECM in the bulk region of PAO1 biofilms presents a dense and mesh-like fibrillar structure, suggesting that the aligned fibrillar organization is typical for the mucoid strain but not ubiquitously observed. PA cells were homogeneously distributed in both types of biofilms.

The observations of aligned fibrillar structures in the interior of mucoid PA biofilms but not in the denser PAO1 biofilms were surprising, as the ECM in mucoid biofilms is distinguished by predominantly being formed from alginate, which has more than an order of magnitude smaller dimensions than the thickness and spacing of the structures observed in our images. Notably, the

well-ordered and aligned fibrillar features are also absent in any of the compositionally comparable alginate hydrogels (**Figures 1A – C**), suggesting that these features observed in mucoid PA biofilms (*cf.* **Figure 6**B) B) do not arise from the alginate matrix alone. Instead, they may reflect biofilm-specific structural organization involving other ECM components that self-assemble or are organized by the mucoid PA during biofilm matrix synthesis. The contrast, size, and organization of the fibrillar features indicate larger bundles, such as could be produced by large glycoconjugates or amyloid protein fibers, which are known ECM components of *Pseudomonas*.[66–68] Their appearance only in the bulk of thick mucoid biofilms seems to reflect the process of biofilm maturation and structural differentiation.

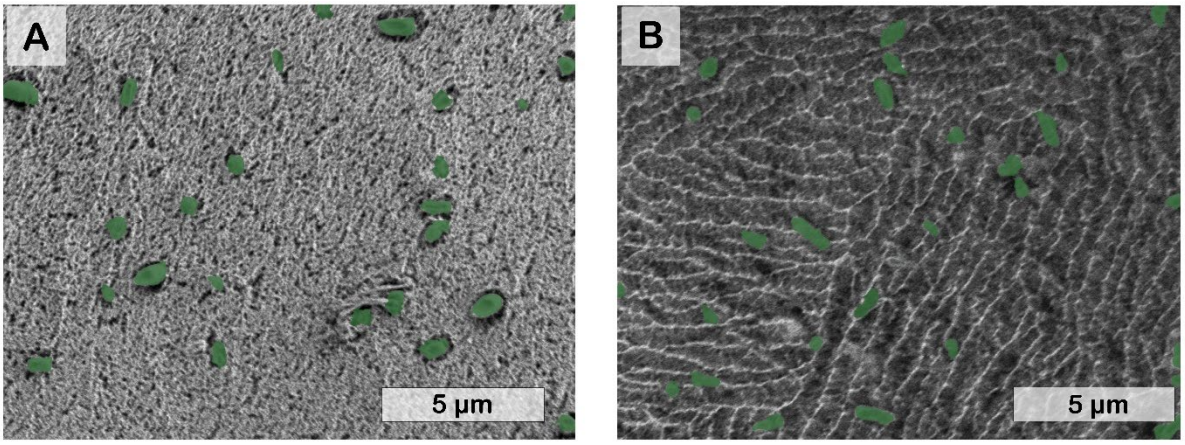

Figure 6: Minimally etched cryo-SEM micrographs of bulk planes from biofilms highlighting differences between 4-day-old PAO1 and mucoid PA biofilms grown on carriers. A) PAO1 biofilms, and B) mucoid PA biofilms

2.5 PAO1 Biofilms Are Thinner with Higher and More Variable Cell Density than Mucoid Biofilms

In addition to imaging the different biofilms grown on carriers (as substrate), we grew biofilms on sapphire discs to obtain a quantitative, cross-sectional view of the native biofilm thickness, bacterial density, and ECM structure as a function of distance from the biofilm substrate. The discs were mounted vertically in the cryo-sample holder (**Figure S3b**) and fractured, allowing for a cross-sectional view orthogonal to the growth surface. This orientation exposes the entire biofilm profile, from base to surface, enabling direct visualization of spatial features such as matrix distribution, bacterial layering, and changes in density along the biofilm depth, as well as the accurate native biofilm thickness. This approach has been used to study biofilm architecture of *Staphylococcus aureus*, *Candida parapsilosis,* and co-cultures of *Staphylococcus epidermidis* and yeast.[22,40]

However, it has not been previously applied to elucidate and compare the matrix and cell organization of PA strains.

When grown on discs, the cross-sectional view of biofilms showed that the ECM of both PAO1 and mucoid PA biofilms formed a thick, cohesive, and uniform mesh-like structure (**Figure 7A and B**). The ECM enveloped the bacterial cells, embedding them within the biofilm and indicating robust matrix production and structural integrity. Despite similarities in matrix appearance, several quantifiable differences were observed in biofilm thickness between the two strains. PAO1 biofilms exhibited a relatively thinner structure, with thicknesses ranging from 20 to 24 µm, while mucoid PA biofilms were thicker (between 45 and 50 µm) after 4 days of growth. This finding is in line with the results from Nahum *et al*.[69] They documented 20% higher thicknesses of 5-day-old mucoid PA biofilms (~ 65 µm) than non-mucoid PA biofilms. [69]The higher thicknesses of mucoid biofilms likely reflect the enhanced production of EPS, which is well documented.[69]

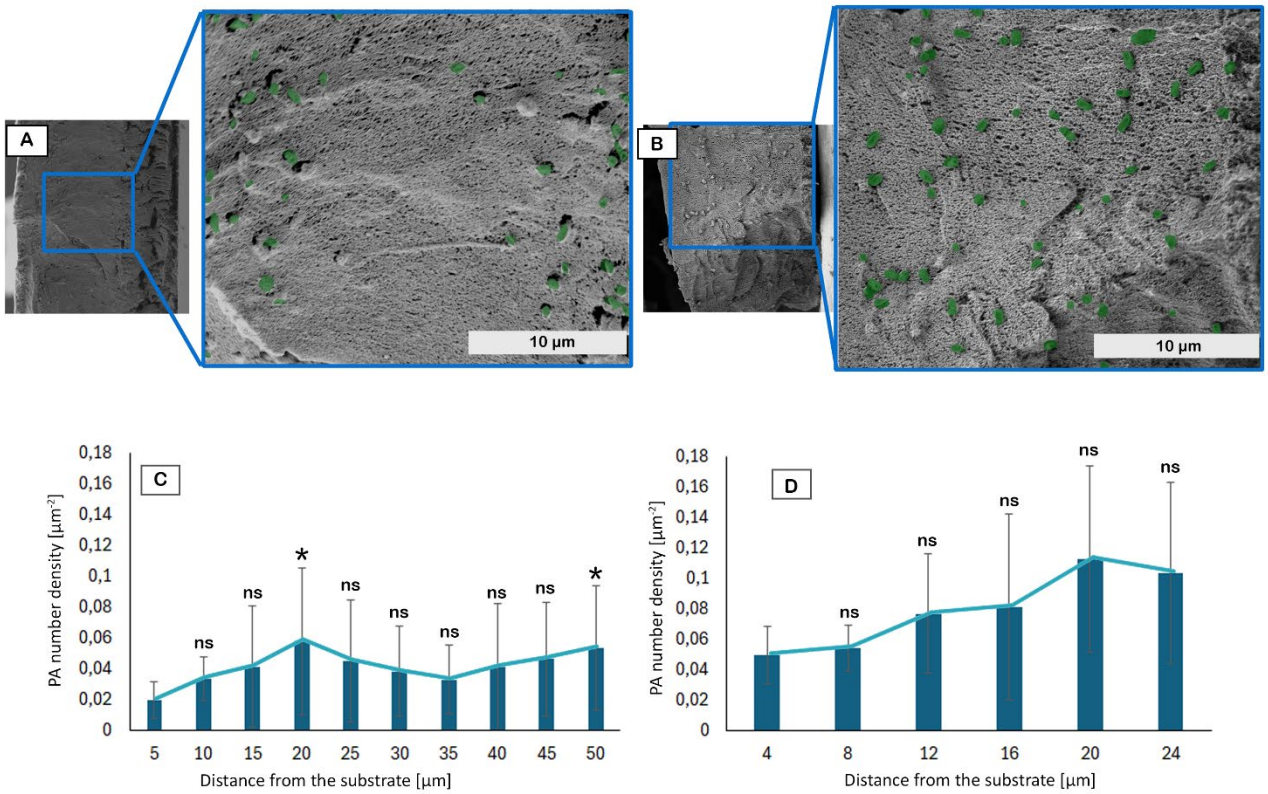

Figure 7: Cryo-SEM micrographs and spatial density profiles of PA biofilms grown on sapphire discs for 4 days and subsequently high-pressure cryo-frozen and fractured orthogonally to the substrate to reveal a biofilm cross-section for (A) Mucoid PA biofilm and B) PAO1 biofilm. Cell density profiles for (C) mucoid PA and (D) PAO1. The first bars in the cell density profiles of mucoid PA (5 µm) and PAO1 (4 µm), respectively, represent the density of cells closest to the

substrate and were used as the control for statistical comparison. Statistical significance was assessed relative to the control. * = $p \leq 0.05$; ns = $p \geq 0.05$

However, cell density varied between the samples, and for mucoid PA biofilms, it was significantly different with distance from the substrate surface. Understanding these vertical cell density gradients is crucial for optimizing treatment strategies targeting biofilm-associated infection. Despite the mucoid biofilm's apparent higher ECM density and thicker structure, the bacteria density in PAO1 biofilms was twice as high ($p \leq 0.05$) compared to the bacteria density in mucoid biofilms **(Figure 7 and S4)**. This suggests that while mucoid PA produces more matrix material and thicker biofilms, PAO1 biofilms are more densely populated.

While several studies have highlighted elevated bacterial densities and metabolic activities at the biofilm-nutrient source interface,[70–73] to our knowledge, no study has reported the bacterial distribution throughout mucoid PA and PAO1 biofilms. In 4-day-old mucoid biofilms, cell densities exhibited a distinct stratified pattern, showing a non-monotonic decrease in bacterial density towards the substrate (sapphire disc). The highest densities (0,053 ± 0,040 μm^{-2}) were observed at the biofilm-liquid interface (distance: ~45–50 µm) and 20 µm away from the surface (0,058 ± 0,048 μm^{-2}). These increased cell densities were ~2.5-fold ($p \leq 0.05$) greater than the density in the zone nearest to the substrate (0,019 ± 0,040 μm^{-2}) (**Figure 7C**). The observed spatial variation in cell density, especially the enrichment of cells near the liquid interface in biofilms, has important implications for biofilm physiology, including differential oxygen penetration, ECM distribution, and antibiotic susceptibility across biofilm layers.

In contrast, PAO1 biofilm cell density averages indicate a monotonic decrease in cell density towards the substrate, accompanied by a decrease in variance (**Figure 7D**). However, the differences in cell densities were statistically insignificant ($p \geq 0.05$) (**Figures 7D and S5B**).

PAO1 consistently showed higher cell densities than the mucoid strain biofilms for the surface, bulk, and bottom regions, respectively (**Figure S6**), leading to the statistically significant difference in overall cell density between PAO1 and mucoid strains (**Figure S4**). However, these inter-strain differences were not statistically significant when compared for each stratum of biofilm separately (**Figure S6**), due to the high variance of the observed cell densities in the PAO1 biofilms.

3. 0 Materials and Methods

3.1 Bacterial strains, growth conditions, and antibiotics.

The *P. aeruginosa* (PA) strains utilized in this study include PAO1(ATCC 15692) and a mucoid strain (ATCC 39324). Unless otherwise specified, frozen bacterial stocks were thawed and initially cultured overnight at 37 °C in Tryptic Soy Broth (TSB). Subsequently, the bacteria were sub-cultured onto Tryptic Soy Agar (TSA) plates and incubated for 24 h. Colonies were then transferred to 10 ml of TSB and cultured at 37 °C for 16–18 h with agitation at 100 rpm to produce a bacterial suspension for further experimentation.

3.2 Biofilm Growth

Overnight cultures of PA strains were harvested and washed 3 times with phosphate-buffered saline (PBS). The bacterial suspensions were then adjusted to an optical density at 600 nm (OD_{600}) of 0.1 in TSB. Sterile 3 mm diameter specimen carriers (gold-coated – Type A, Leica Microsystems Inc., Austria) (**Figure S3a**) with 100 µm indentations, along with 6 mm sapphire discs (Leica Microsystems Inc., Austria) (**Figure S3b**), were placed in Petri dishes containing the respective bacterial (PAO1 & PA ATCC 39324) suspensions. Unless otherwise stated, PA strains were allowed to grow for 4 days in TSB to form biofilms on these substrates by incubating them at 37 °C. After growth, biofilms were covered with an additional 3 mm or 6 mm Type A carrier, carefully lined with double-sided tape to create a secure sandwich.

3.3 Alginate hydrogel preparation

A 1.5 wt% alginate stock solution (acetylated)[9] was prepared by dissolving 150 mg alginate overnight in 8 ml of sterile 0.9 wt% NaCl solution (solvent). Then, the solvent was added to the mixture to achieve a final volume of 10 mL, which was used as the stock solution. For alginate gels containing bacteria, the stock solution was diluted with 0.9 wt% NaCl and PAO1 liquid culture to obtain a 0.5 wt% alginate solution as ink with a defined PA concentration (0.1 OD).

Approximately 150 µl of PA-containing and control (without PA) alginate solutions were then placed in disc-shaped agarose molds. To prepare agarose molds, 2 g of agarose powder (Sigma) was mixed with 1.47 g of $CaCl_2$ in 100 mL of Milli-Q water and then autoclaved. The agarose molds were gelled to a height of 3 mm and punctured with 7-mm-diameter punches. For alginate hydrogel fabrication, the punched spaces in the agarose molds were filled with PA-containing and control alginate solutions, respectively. The solutions were left to crosslink in the agarose molds at room temperature for 1 h. After gelling, the hydrogels were washed three times with 0.9 wt% NaCl.

Hydrogels with PA were incubated in $CaCl_2$-supplemented TSB overnight at 37 °C under shaking at 100 rpm.

3.4 Sample Preparation for SEM Imaging

3.4.1 Air/HDMS Drying and Scanning Electron Microscope Imaging of Samples

Alginate hydrogels and PA biofilms, after incubation, were subjected to chemical fixation by immersion in a 2.5% glutaraldehyde solution (Sigma) and left overnight at 4 °C. Following fixation, the samples underwent two consecutive rinses with a 0.9 wt% sodium chloride (NaCl) solution, followed by sequential dehydration in ethanol solutions of increasing concentrations: 30%, 50%, 70%, 90%, 95%, and finally, 100%, all conducted at room temperature for 3 min each. Subsequently, the chemically fixed samples were treated with 100% hexamethyldisilazane (HMDS) for 1 min and air-dried. Before the biofilm samples grown in carriers were air-dried, they were fractured manually with a blade, while the alginate hydrogel samples were sliced in half with a blade after air-drying. All samples were uniformly sputter-coated (Leica EM SCD005, Leica, Germany) with a ~8 nm thick layer of gold to enhance sample conductivity and image contrast. SEM imaging was carried out using an Apreo VS SEM (Thermo Scientific, The Netherlands) at an acceleration voltage of 5.0 kV and a current of 0.10 nA. High vacuum back-scattered and secondary electrons were detected using T1 and T2 in-lens detectors, respectively.

3.4.2 Critical-point Drying and Scanning Electron Microscope Imaging of Samples

Alginate hydrogels and PA biofilms were subjected to chemical fixation and dehydration as described above. Subsequently, samples were transitioned to acetone (Sigma) as the intermediary solvent before drying using a critical-point dryer (Leica EM CPD030, Leica, Germany). Samples were sliced in half with a blade and subsequently coated with ~8 nm of gold, and then imaged with SEM (Apreo VS SEM, Thermo Scientific, The Netherlands).

3.4.3 Cyro preparation and Scanning Electron Microscope Imaging of Samples

Selected samples were high-pressure frozen using the Leica EM HPM100 (Leica Microsystems Inc., Austria). More specifically, for PA-containing and empty alginate hydrogels, ~80–100 µm thick slices were cut with a sterile scalpel and transferred to the bottom carrier using forceps and then sandwiched with a top carrier. For PA biofilms, samples on the 3 mm Type A carriers were gently covered with matching top carriers to create a secure sandwich. The sapphire discs with biofilms were placed (biofilm side up) into the indentation of a 6 mm Type A carrier. A spacer was added on top to prevent movement and ensure even contact. The assembly is completed by placing a matching top carrier over the disc to create a secure sandwich.

All sandwiched carriers are immediately loaded into the HPM100 high-pressure freezer and automatically frozen according to the protocol described in Garbarino et al.[57] The frozen samples are afterwards discharged into a liquid nitrogen-filled Dewar for preservation before being transferred to the freeze-fracture system under cryogenic conditions. The frozen sample carriers or sapphire discs were mounted onto the sample holder under liquid nitrogen (LN_2) and transferred to a Leica EM ACE900 (Leica Microsystems Inc., Austria) freeze-fracture system. Freeze-fracturing was performed at -120 °C using a flat-edge knife.

Unless otherwise stated, to enhance structural visibility of fractured samples, sublimation (etching) was performed for 20 s at –110 °C under a vacuum of ~5.6×10^{-7} mbar. While a standard etching time of 20 s was applied for most samples, selected samples were also subjected to 0 s (no sublimation) and extended 60 s etching times. This approach enabled the assessment of surface exposure of the ECM and bacterial structure.

Following the sublimation step, the fractured samples were e-beam coated with a 4-nm platinum layer at a 45° angle and a 4-nm carbon layer at a 90° angle to improve contrast and minimize beam damage during imaging. Subsequently, the samples were transferred to SEM via a cryo-transfer system (Leica EM VCT500).

Cryo-SEM imaging was performed using the Apreo VS SEM (Thermo Scientific, The Netherlands) at an operating voltage of 1.0 kV and a current of 0.10 nA in a high vacuum mode. Backscattered and secondary electrons were detected via the in-lens T1 and T2 detectors, respectively. Throughout the imaging process, the SEM chamber temperature was maintained between -110 °C and -120 °C, depending on the chamber pressure to avoid sublimation and condensation, as observed *in situ*.

For each imaging technique, more than three independent samples were prepared. From each sample, a minimum of 10 fields of view were imaged, and representative images were selected based on the preservation of sample structures. Where applicable, bacterial cells were manually false-coloured green using Adobe Photoshop (version 25.5.3).

3.5 Quantitative Spatial Analysis of *Pseudomonas* Biofilm Structure

3.5.1 Radial Distribution Function (RDF) Analysis

To assess spatial clustering within the plane of biofilms grown in carriers, the cryo-SEM images were manually annotated with disk markers to represent individual bacterial cells. This was necessary because the dense biofilm architecture hindered reliable automated detection with image analysis software like ImageJ. Disk-annotated images were processed using a home-written Python script that extracted the centroid positions of each annotated bacterium. Each image was processed, correcting for edge effects up to a radius parameter of 40% of the image height to calculate the

radial distribution function, g(r). The g(r) for each image of the same type of sample was aggregated, and the standard error of the mean (SEM) and 95% confidence intervals (assuming Student's t-test) for each distance bin were calculated. The nearest-neighbor (first order) peak was fitted with a Gaussian by assuming a g(r) = 1 background and a peak in the interval from the cross-over g(r) >1 to g(r) < 1.1.

3.5.2 Vertical Cell Density Profiling in Cryo-Imaged Biofilms

To evaluate how cell density varied with distance from the substrate, fractured biofilms grown on sapphire discs were analyzed. Each image was divided into horizontal rectangular regions of interest (ROIs), aligned parallel to the substrate. For mucoid biofilms, ROI widths were set to 5 µm, while for PAO1 biofilms, a width of 4 µm was used to accommodate differences in biofilm structure and cell density. Cell counts within each ROI were determined manually using Adobe Photoshop, allowing for consistent and accurate quantification. The constant area across ROIs enabled direct calculation of cell density (cells per μm^2) as a function of distance from the substrate. For statistical evaluation, mean cell density and standard deviation were calculated for each ROI bin. One-way ANOVA with Tukey and LSD post hoc tests was performed to determine significant differences in cell density across depths. (IBM SPSS Statistics (27.0.1)). A p-value ≤ 0.05 was considered statistically significant.

3.5.3 Pore Size Distribution of Acetylated Alginate Prepared by Different Methods

SEM micrographs of the acetylated alginate samples prepared by air-drying, CPD, and cryo methods were taken at similar magnifications to ensure consistent pore size measurements. Pore size analysis was conducted using ImageJ. The measured pores were saved in CSV format, and the resulting datasets were imported into RStudio (version R4.3.1, R Foundation for Statistical Computing) for statistical analysis and visualization. Pore size distributions for each preparation method were visualized using boxplots, generated with the ggplot2 package, to illustrate the variation in pore dimensions across sample groups. Results are reported as mean ± standard deviation and were analyzed using one-way ANOVA with Tukey and LSD post hoc tests (IBM SPSS Statistics (27.0.1)), to determine significant differences.

4. Conclusion

Using a cryo-SEM workflow, we revealed 4-day-old *Pseudomonas* biofilms as highly hydrated, spatially organized structures, with individual bacteria distinctly embedded within the extracellular matrix. The imaged structures stood in stark contrast to the dense, clustered bacterial arrangements reported for samples prepared by conventional air-drying or critical-point drying methods. Clusters

and microcolonies were absent in both mucoid PA and PAO1 biofilms. Cross-section comparisons between mucoid and PAO1 4-day-old biofilms revealed that PAO1 biofilms are only half as thick. By quantitative analysis of cryo-SEM images, we determined that mucoid PA biofilms exhibit short-range order with clear separation and a uniform nearest-neighbor spacing of ~1.25 µm throughout the biofilm. Furthermore, using cross-section freeze-fracture cryo-SEM, we demonstrated that the bacterial density distribution in mucoid biofilms is relatively uniform, but significantly higher at the top of the biofilm than close to the substrate. While PAO1 biofilms had twice the cell density of mucoid PA, tentatively increasing from the substrate to the surface, they also display much higher variability and lack a clear nearest-neighbor distance and gap distance.
Finally, we imaged aligned fibrillar structures in the bulk of mucoid PA biofilms. Such structures were not found in pure alginate hydrogels nor in PAO1 biofilms. We suggest that they originate from proteins, such as amyloid fibrils or large glycoconjugates that can organize in the mucoid alginate-rich matrix during maturation, but further analyses are needed to confirm this hypothesis.
Our study highlights the critical importance of selecting appropriate sample preparation methods for accurately visualizing native biofilm structures and the potential for using cryo-SEM as a quantitative tool for biofilm analysis, thanks to its preservation of features and distances from the native state. Importantly, it can offer insights into the considerable structural variability in biofilm organization that we demonstrated persists even between strains.

Funding

We thank the FWF Austrian Science Fund for funding (P33226).

References

1. Hoiby, N., Ciofu, O. & Bjarnsholt, T. *Pseudomonas aeruginosa* Biofilms in Cystic fibrosis. *Future Microbiol* **5**, 1663–1674 (2010).
2. Wei, Q. & Ma, L. Biofilm Matrix and Its Regulation in *Pseudomonas aeruginosa*. *Int J Mol Sci* **14**, 20983–21005 (2013).
3. Thi, M. T. T., Wibowo, D. & Rehm, B. H. A. *Pseudomonas aeruginosa* Biofilms. *Int J Mol Sci* **21**, 8671 (2020).
4. Guillaume, O., Butnarasu, C., Visentin, S. & Reimhult, E. Interplay between biofilm microenvironment and pathogenicity of *Pseudomonas aeruginosa* in cystic fibrosis lung chronic infection. *Biofilm* vol. 4 Preprint at https://doi.org/10.1016/j.bioflm.2022.100089 (2022).

5. Ghafoor, A., Hay, I. D. & Rehm, B. H. A. Role of Exopolysaccharides in *Pseudomonas aeruginosa* Biofilm Formation and Architecture. *Appl Environ Microbiol* **77**, 5238–5246 (2011).
6. Kundukad, B., Rice, S. A., Doyle, P. S. & Kjelleberg, S. Alginate exopolymer significantly modulates the viscoelastic properties and resilience of bacterial biofilms. *NPJ Biofilms Microbiomes* **11**, 98 (2025).
7. Hentzer, M. *et al.* Alginate Overproduction Affects *Pseudomonas aeruginosa* Biofilm Structure and Function. *J Bacteriol* **183**, 5395–5401 (2001).
8. Boyd, A. & Chakrabarty, A. M. *Pseudomonas aeruginosa* biofilms: role of the alginate exopolysaccharide. *J Ind Microbiol* **15**, 162–168 (1995).
9. Schandl, S. *et al.* Acetylation of alginate enables the production of inks that mimic the chemical properties of *P. aeruginosa* biofilm. *J Mater Chem B* (2025) doi:10.1039/d4tb02675f.
10. Sønderholm, M. *et al.* Tools for studying growth patterns and chemical dynamics of aggregated *Pseudomonas aeruginosa* exposed to different electron acceptors in an alginate bead model. *NPJ Biofilms Microbiomes* **4**, 3 (2018).
11. Li, S. *et al.* Hierarchical biofilm models using sodium alginate beads containing bacteria embedded in a cellulose–chitosan hydrogel matrix. *J Mater Chem B* **13**, 3952–3958 (2025).
12. Cao, B. *et al.* Antibiotic penetration and bacterial killing in a *Pseudomonas aeruginosa* biofilm model. *Journal of Antimicrobial Chemotherapy* **70**, 2057–2063 (2015).
13. Park, J. *et al.* Direct Observation of Wet Biological Samples by Graphene Liquid Cell Transmission Electron Microscopy. *Nano Lett* **15**, 4737–4744 (2015).
14. Ogura, T. Direct observation of unstained biological samples in water using newly developed impedance scanning electron microscopy. *PLoS One* **14**, e0221296 (2019).
15. Lyu, Z., Yao, L., Chen, W., Kalutantirige, F. C. & Chen, Q. Electron Microscopy Studies of Soft Nanomaterials. *Chem Rev* **123**, 4051–4145 (2023).
16. Asker, D. *et al.* Preventing *Pseudomonas aeruginosa* Biofilms on Indwelling Catheters by Surface-Bound Enzymes. *ACS Appl Bio Mater* **4**, 8248–8258 (2021).
17. Manabe, K., Nishizawa, S. & Shiratori, S. Porous Surface Structure Fabricated by Breath Figures that Suppresses *Pseudomonas aeruginosa* Biofilm Formation. *ACS Appl Mater Interfaces* **5**, 11900–11905 (2013).
18. Sugimoto, S. *et al.* Imaging of bacterial multicellular behaviour in biofilms in liquid by atmospheric scanning electron microscopy. *Sci Rep* **6**, 25889 (2016).

19. Relucenti, M. *et al.* Microscopy Methods for Biofilm Imaging: Focus on SEM and VP-SEM Pros and Cons. *Biology (Basel)* **10**, 51 (2021).
20. Asahi, Y. *et al.* Simple observation of *Streptococcus mutans* biofilm by scanning electron microscopy using ionic liquids. *AMB Express* **5**, 6 (2015).
21. Alleman, J. E., Russell, E. K., Lantz, W. L. & Wukasch, R. F. Biofilm cryopreparation for scanning electron microscopy. *Water Res* **19**, 1073–1078 (1985).
22. Hrubanova, K., Nebesarova, J., Ruzicka, F. & Krzyzanek, V. The innovation of cryo-SEM freeze-fracturing methodology demonstrated on high pressure frozen biofilm. *Micron* **110**, 28–35 (2018).
23. Fleeman, R. M., Mikesh, M. & Davies, B. W. Investigating *Klebsiella pneumoniae* biofilm preservation for scanning electron microscopy. *Access Microbiol* **5**, (2023).
24. Schaudinn, C. *et al.* Imaging of endodontic biofilms by combined microscopy (FISH/cLSM – SEM). *J Microsc* **235**, 124–127 (2009).
25. Priester, J. H. *et al.* Enhanced visualization of microbial biofilms by staining and environmental scanning electron microscopy. *J Microbiol Methods* **68**, 577–587 (2007).
26. Lawrence, J. R. *et al.* Scanning Transmission X-Ray, Laser Scanning, and Transmission Electron Microscopy Mapping of the Exopolymeric Matrix of Microbial Biofilms. *Appl Environ Microbiol* **69**, 5543–5554 (2003).
27. Kher, L., Kelley, K. & Santoro, D. Ultrastructural Analysis of Differences in the Growth and Maturation of *Staphylococcus pseudintermedius* Biofilm on Biotic and Abiotic Surfaces. *Microbiol Spectr* **11**, (2023).
28. Zhang, Y. *et al.* Challenges and current advances in in vitro biofilm characterization. *Biotechnol J* **18**, (2023).
29. Fratesi, S. E., Lynch, F. L., Kirkland, B. L. & Brown, L. R. Effects of SEM Preparation Techniques on the Appearance of Bacteria and Biofilms in the Carter Sandstone. *Journal of Sedimentary Research* **74**, 858–867 (2004).
30. Kang, K.-Y. *et al.* Critical Point Drying: An Effective Drying Method for Direct Measurement of the Surface Area of a Pretreated Cellulosic Biomass. *Polymers (Basel)* **10**, 676 (2018).
31. Dassanayake, R. P. *et al.* Identification of a reliable fixative solution to preserve the complex architecture of bacterial biofilms for scanning electron microscopy evaluation. *PLoS One* **15**, e0233973 (2020).

32. Karcz, J., Bernas, T., Nowak, A., Talik, E. & Woznica, A. Application of lyophilization to prepare the nitrifying bacterial biofilm for imaging with scanning electron microscopy. *Scanning* **34**, 26–36 (2012).
33. Johnson, E. *et al.* Correlative in-resin super-resolution and electron microscopy using standard fluorescent proteins. *Sci Rep* **5**, 9583 (2015).
34. McCutcheon, J. & Southam, G. Advanced biofilm staining techniques for TEM and SEM in geomicrobiology: Implications for visualizing EPS architecture, mineral nucleation, and microfossil generation. *Chem Geol* **498**, 115–127 (2018).
35. Hrubanova, K., Nebesarova, J., Ruzicka, F. & Krzyzanek, V. The innovation of cryo-SEM freeze-fracturing methodology demonstrated on high pressure frozen biofilm. *Micron* **110**, 28–35 (2018).
36. Ichihashi, S., Kuwata, M., Kikuchi, K., Matsuyama, T. & Shimizu, A. Optimization of method for cross-section hydrogels preparation using high-pressure freezing. *Microscopy* **73**, 430–438 (2024).
37. Kristensen, G. & Christensen, F. Application of cryo-cut method for measurements of biofilm thickness. *Water Res* **16**, 1619–1621 (1982).
38. Webster, P., Wu, S., Webster, S., Rich, K. A. & McDonald, K. Ultrastructural preservation of biofilms formed by non-typeable *Hemophilus influenzae*. *Biofilms* **1**, 165–182 (2004).
39. Wan, P. *et al.* Cryo-SEM Investigation of Chlorella Using Filter Paper as Substrate. *Bio Protoc* **14**, (2024).
40. Krzyzanek, V., Hrubanova, K., Nebesarova, J. & Ruzicka, F. Cryo-SEM of Perpendicular Cross Freeze-Fractures Through a High-Pressure-frozen Biofilm. *Microscopy and Microanalysis* **20**, 1232–1233 (2014).
41. Osondu-Chuka O.G., Schandl. S., Scheberl. A., Guillaume. O., Ovsianikov. A., & Reimhult. E. Beyond the Matrix: Rethinking Antibiotic Tolerance in CF Biofilms Using 3D Models. *Npj Biofilms and Microbiomes*- submitted (2025).
42. Sønderholm, M. *et al.* Pseudomonas aeruginosa Aggregate Formation in an Alginate Bead Model System Exhibits *In Vivo* -Like Characteristics. *Appl Environ Microbiol* **83**, (2017).
43. Wright, B. *et al.* Enhanced Viability of Corneal Epithelial Cells for Efficient Transport/Storage Using a Structurally Modified Calcium Alginate Hydrogel. *Regenerative Med* **7**, 295–307 (2012).
44. Schandl, S. *et al.* Synthetically acetylated alginate is a superior in vitro biofilm model for antibiotic testing showing reduced tobramycin affinity. *Eur Polym J* **237**, 114176 (2025).

45. Fratesi, S. E., Lynch, F. L., Kirkland, B. L. & Brown, L. R. Effects of sem preparation techniques on the appearance of bacteria and biofilms in the carter sandstone. Journal of sedimentary research vol. 74 (2004).
46. Azeredo, J. *et al.* Critical review on biofilm methods. *Crit Rev Microbiol* **43**, 313–351 (2017).
47. Alhede, M. *et al.* Combination of microscopic techniques reveals a comprehensive visual impression of biofilm structure and composition. *FEMS Immunol Med Microbiol* **65**, 335–342 (2012).
48. Zhang, Q. *et al.* Morphogenesis and cell ordering in confined bacterial biofilms. *Proceedings of the National Academy of Sciences* **118**, (2021).
49. Tolker-Nielsen, T. & Molin, S. Spatial Organization of Microbial Biofilm Communities. *Microb Ecol* **40**, 75–84 (2000).
50. Hobley, L., Harkins, C., MacPhee, C. E. & Stanley-Wall, N. R. Giving structure to the biofilm matrix: an overview of individual strategies and emerging common themes. *FEMS Microbiol Rev* **39**, 649–669 (2015).
51. Li, D. *et al.* Biofilm Formation by Pseudomonas aeruginosa in a Novel Septic Arthritis Model. *Front Cell Infect Microbiol* **11**, (2021).
52. Yang, Y. *et al.* Inactivation of Pseudomonas aeruginosa Biofilms by 405-Nanometer-Light-Emitting Diode Illumination. *Appl Environ Microbiol* **86**, (2020).
53. Lee, K. & Yoon, S. S. Pseudomonas aeruginosa Biofilm, a Programmed Bacterial Life for Fitness. *J Microbiol Biotechnol* **27**, 1053–1064 (2017).
54. Brandenburg, K. S. *et al.* Development of *Pseudomonas aeruginosa* Biofilms in Partial-Thickness Burn Wounds Using a Sprague-Dawley Rat Model. *Journal of Burn Care & Research* **40**, 44–57 (2019).
55. Wan, P. *et al.* Cryo-SEM Investigation of Chlorella Using Filter Paper as Substrate. *Bio Protoc* **14**, (2024).
56. Dohnalkova, A. C. *et al.* Imaging Hydrated Microbial Extracellular Polymers: Comparative Analysis by Electron Microscopy. *Appl Environ Microbiol* **77**, 1254–1262 (2011).
57. Garbarino, E., Subbiahdoss, G., Scheberl, A., Reimhult, E. & Misevic, G. The native glycocalyx ultrastructure in humans and sponges is a self-assembled, lamellar micro- and nanoarray. *Commun Biol* **7**, 1677 (2024).
58. Hills, O. J., Smith, J., Scott, A. J., Devine, D. A. & Chappell, H. F. Cation complexation by mucoid Pseudomonas aeruginosa extracellular polysaccharide. *PLoS One* **16**, e0257026 (2021).

59. Płókarz, D., Czopowicz, M., Bierowiec, K. & Rypuła, K. Virulence Genes as Markers for Pseudomonas aeruginosa Biofilm Formation in Dogs and Cats. *Animals* **12**, 422 (2022).
60. Maurice, N. M., Bedi, B. & Sadikot, R. T. *Pseudomonas aeruginosa* Biofilms: Host Response and Clinical Implications in Lung Infections. *Am J Respir Cell Mol Biol* **58**, 428–439 (2018).
61. Jacobs, H. M. *et al.* Mucoid Pseudomonas aeruginosa Can Produce Calcium-Gelled Biofilms Independent of the Matrix Components Psl and CdrA. *J Bacteriol* **204**, (2022).
62. Thi, M. T. T., Wibowo, D. & Rehm, B. H. A. Pseudomonas aeruginosa Biofilms. *Int J Mol Sci* **21**, 8671 (2020).
63. Yin, R., Cheng, J., Wang, J., Li, P. & Lin, J. Treatment of Pseudomonas aeruginosa infectious biofilms: Challenges and strategies. *Front Microbiol* **13**, (2022).
64. Hunter, R. C. & Beveridge, T. J. High-Resolution Visualization of *Pseudomonas aeruginosa* PAO1 Biofilms by Freeze-Substitution Transmission Electron Microscopy. *J Bacteriol* **187**, 7619–7630 (2005).
65. Wilking, J. N., Angelini, T. E., Seminara, A., Brenner, M. P. & Weitz, D. A. Biofilms as complex fluids. *MRS Bull* **36**, 385–391 (2011).
66. Nahum, Y., Cerrone, A. & Nerenberg, R. Impact of Low-Frequency Ultrasound on Physical Properties and Antibiotic Susceptibility of a Mucoid Biofilm. *Langmuir* **41**, 6718–6728 (2025).
67. Zeng, G. *et al.* Functional bacterial amyloid increases Pseudomonas biofilm hydrophobicity and stiffness. *Front Microbiol* **6**, (2015).
68. Bleem, A. *et al.* Protein Engineering Reveals Mechanisms of Functional Amyloid Formation in Pseudomonas aeruginosa Biofilms. *J Mol Biol* **430**, 3751–3763 (2018).
69. Nahum, Y., Cerrone, A. & Nerenberg, R. Impact of Low-Frequency Ultrasound on Physical Properties and Antibiotic Susceptibility of a Mucoid Biofilm. *Langmuir* **41**, 6718–6728 (2025).
70. Werner, E. *et al.* Stratified Growth in *Pseudomonas aeruginosa* Biofilms. *Appl Environ Microbiol* **70**, 6188–6196 (2004).
71. Sternberg, C. *et al.* Distribution of Bacterial Growth Activity in Flow-Chamber Biofilms. *Appl Environ Microbiol* **65**, 4108–4117 (1999).
72. Wentland, E. J., Stewart, P. S., Huang, C.-T. & McFeters, G. A. Spatial Variations in Growth Rate within Klebsiella pneumoniae Colonies and Biofilm. *Biotechnol Prog* **12**, 316–321 (1996).

73. Xu, K. D., McFeters, G. A. & Stewart, P. S. Biofilm resistance to antimicrobial agents. *Microbiology (N Y)* **146**, 547–549 (2000).